

Autoregressive neural-network wavefunctions for *ab initio* quantum chemistry

Thomas D. Barrett,^{1,2,*} Aleksei Malyshev,¹ and A. I. Lvovsky^{1,3,†}

¹University of Oxford, Clarendon Laboratory, Parks Road, Oxford, OX1 3PU, UK

²InstaDeep, London, W2 6LG, UK

³Russian Quantum Center, Skolkovo, 143025, Moscow, Russia

Performing electronic structure calculations is a canonical many-body problem that has recently emerged as a challenging new paradigm for neural network quantum states (NNQS). Here, we parameterise the electronic wavefunction with a novel autoregressive neural network (ARN) that permits highly efficient and scalable sampling, whilst also embedding physical priors that reflect the structure of molecular systems without sacrificing expressibility. This allows us to perform electronic structure calculations on molecules with up to 30 spin-orbitals — which consider multiple orders of magnitude more Slater determinants than previous applications of conventional NNQS — and we find that our ansatz can outperform the de-facto gold-standard coupled cluster methods even in the presence of strong quantum correlations. With a highly expressive neural network for which sampling is no longer a computational bottleneck, we conclude that the barriers to further scaling are not associated with the wavefunction ansatz itself, but rather are inherent to any variational Monte Carlo approach.

I. INTRODUCTION

The grand challenge of *ab initio* quantum chemistry (QC) is to solve the many-body Schrödinger equation describing interaction of heavy nuclei and orbiting electrons. In principle, such solutions can provide complete access to a molecular entity’s chemical properties, however, in practice, the remarkable complexity of these systems makes them intractable for all but the simplest of cases. Indeed, the many-body electronic problem is fundamentally NP-hard [1], which has motivated significant efforts to tailor numerical methods to QC systems [2–4].

The QC task we pursue here is to find the ground state of a molecular system containing N_e electrons. Under the Born-Oppenheimer approximation — which treats the nuclei as classical point charges — the molecular Hamiltonian can be written (using atomic units) in the position basis as [5]

$$\mathcal{H} = -\sum_i \frac{\nabla_i^2}{2} - \sum_{i,I} \frac{Z_I}{|\mathbf{r}_i - \mathbf{R}_I|} + \frac{1}{2} \sum_{i \neq j} \frac{1}{|\mathbf{r}_i - \mathbf{r}_j|}. \quad (1)$$

with \mathbf{r}_i being the spatial position of the i -th electron, \mathbf{R}_I and Z_I denoting the position and atomic number of the I -th nucleus. The state of interest satisfies the time-independent Schrödinger equation

$$\mathcal{H}|\psi\rangle = E|\psi\rangle \quad (2)$$

and its wavefunction $\langle \xi_1, \dots, \xi_{N_e} | \psi \rangle = \psi(\xi_1, \dots, \xi_{N_e})$ is represented in coordinates $\xi_i = (m_{s,i}, \mathbf{r}_i)$, which include both the spin projection and spatial position of the electron. Importantly, the fermionic nature of electrons means that the wavefunction

must obey antisymmetric exchange symmetries, i.e. $\psi(\dots, \xi_i, \dots, \xi_j, \dots) = -\psi(\dots, \xi_j, \dots, \xi_i, \dots)$.

QC methods typically define a basis set of $N_O > N_e$ single-electron spin-orbitals, $\{\chi_i(\xi)\}_{i=1, \dots, N_O}$ and represent the electronic state as a linear combination of the form

$$|\psi\rangle = \sum_k \psi_k |\mathbf{x}_k\rangle, \quad (3)$$

where each of the components $|\mathbf{x}_k\rangle$ is uniquely identified by the subset of basis spin-orbitals that are occupied by an electron. In the second quantization, these components are written as occupation vectors,

$$|\mathbf{x}_k\rangle \equiv |x_k^1, \dots, x_k^{N_O}\rangle, \quad (4)$$

where $x_k^j \in \{0, 1\}$ denotes whether the j -th spin-orbital of the k -th component is occupied, with $\sum_{j=1}^{N_O} x_k^j = N_e \forall k$. In the first quantization, these components are represented by antisymmetric tensor products of the N_e occupied orbitals [5], hence we hereafter refer to them as “(Slater) determinants” and the corresponding sequences \mathbf{x}_k as “configuration strings”.

As the number of possible determinants grows exponentially with the system size, so-called “full configuration interaction” (FCI) methods — those considering the entire space of Slater determinants — rapidly become intractable for growing system sizes.

To combat this scaling issue, leading *ab-initio* QC approaches often consider systematic corrections to a reference state (typically the Hartree-Fock state, the single lowest energy Slater determinant). Configuration interaction (CI) methods [6] restrict the active space to configuration strings that are different from the reference by no more than a certain number of excitations. By contrast, coupled cluster (CC) approaches [7, 8] can access arbitrarily excited Slater determinants using non-linear combinations of excitation operators up to a certain order, but cannot parameterise arbitrary superpositions (i.e. do not offer fully general ψ_k ’s in Eq. (3)).

* t.barrett@instadeep.com

† alex.lvovsky@physics.ox.ac.uk

Whilst both methods trade off expressibility for reduced complexity, they are specifically designed for the typical structure of molecular wavefunctions and often provide good performance. However, even the more accurate CC approach — which is often considered the leading *ab-initio* method — still fails in the presence of strong quantum correlations (i.e. when the wavefunction can no longer be adequately described by systematic corrections to a reference). An alternative is to use compact parameterisations of the electronic wavefunction — such as the Jastrow-Slater ansatz [9] or matrix-product states [10, 11] — which can then be optimised to find the ground state using stochastic [12] or non-stochastic [13] methods.

The limitations of these approaches are typically determined by the expressiveness of the wavefunction ansatz and the efficiency with which it can be optimised, and it is here that machine learning (ML) offers great potential. The approach is based on the assumption that the ground state is dominated by relatively few ($K \ll \binom{N_o}{N_e}$) Slater determinants. A generative neural network, with parameters θ , can encode the molecular wavefunction and produce *samples* of Slater determinants \mathbf{x}_k with the (*a priori* unknown) probabilities $|\psi_\theta(\mathbf{x}_k)|^2$. A batch of N (where $K \ll N \ll \binom{N_o}{N_e}$) samples, with the associated phases typically determined by an auxiliary network, then constitutes a reasonably accurate approximation of that wavefunction. Standard iterative methods can then be used to optimize the neural network parameters in order to yield the lowest energy expectation value.

In 2017, Carleo and Troyer demonstrated that neural networks — specifically an energy-based model called a restricted Boltzmann machine (RBM) — can parameterise a many-body wavefunction and capture non-trivial correlations within the exponentially large encoded Hilbert space [14]. Subsequently, neural network quantum states (NNQS) have proven to be successful variational ansatz for problems such as finding the ground state of interacting spin-systems [15, 16], quantum state tomography [17–20] and classical simulations of quantum computing [21]. Whilst most of the development of NNQS has been within the context of condensed matter physics (CMP), recently (2020) Choo *et al.* [22] demonstrated that the fermionic electronic structure problem can be mapped to an equivalent optimisation problem on a system of interacting spins, opening the door to applying NNQS to QC. However, RBM models rely on inherently inefficient sampling procedures — such as Markov Chain Monte Carlo (MCMC) methods — to approximate the encoded Boltzmann distribution during training. Moreover, RBMs are a true “black-box” that does not reflect our significant physical knowledge of molecular systems. In this context, the search for alternative neural network architectures that overcome these shortcomings remains an important item on the agenda of this developing field.

In this work we present a novel neural network ansatz for second-quantised molecular wavefunctions that addresses these outstanding challenges. By considering

an autoregressive decomposition of the wavefunction, we demonstrate a highly efficient sampling algorithm, which is inherently parallelised and scales with the number of unique configuration strings sampled instead of the overall sample batch size. The feedforward architecture used allows us to train the network using standard backpropagation techniques [23] and, moreover, embed important physical priors (i.e. conserved quantities and invariances) into the wavefunction without sacrificing expressibility. Ultimately, this allows us to surpass classical CI and CC methods and approach the true FCI solution on systems multiple orders of magnitude beyond what was previously achieved using a conventional NNQS. More broadly, our work represents an ambitious application of NNQS to a challenging system where conventional approaches can fail, which is an important milestone for the field as it progresses from its nascent promise and theoretical investigations [24], to tackling a broader range of problems in quantum many-body physics [25].

II. NEURAL NETWORK WAVEFUNCTION

A. Variational Monte-Carlo optimization

We employ the Jordan-Wigner encoding [26] which treats the state (3) as an ensemble of interacting qubits. The Hamiltonian (1) then takes the form (see Methods for details)

$$\mathcal{H}_Q = \sum_j h_j \prod_{i=1}^{N_Q} \sigma_i^{\nu_{j,i}}, \quad (5)$$

where $\sigma_i^{\nu_{j,i}}$ is a Pauli operator acting on the i -th qubit ($\nu_{j,i} \in \{I, x, y, z\}$). Whilst such a model is often considered as a system of interacting spins in CMP, we will henceforth refer to qubits and reserve “spin” exclusively for the spin-state of electrons to avoid confusion.

Let the component amplitudes of the state (3) depend on a set of ansatz parameters, θ , such that

$$|\psi_\theta\rangle = \sum_k \psi_\theta(\mathbf{x}_k) |\mathbf{x}_k\rangle. \quad (6)$$

This wavefunction can be optimized (trained) to find the ground state of the electronic system using a variational Monte-Carlo (VMC) approach [22]. The energy expectation value is given by

$$E = \langle \psi_\theta | \mathcal{H}_Q | \psi_\theta \rangle = \sum_k E_{\text{loc}}(\mathbf{x}_k) |\psi_\theta(\mathbf{x}_k)|^2, \quad (7)$$

where we have defined the “local energy” of a given Slater determinant as

$$E_{\text{loc}}(\mathbf{x}_k) = \sum_{k'} \frac{\psi_\theta(\mathbf{x}_{k'})}{\psi_\theta(\mathbf{x}_k)} \langle \mathbf{x}_k | \mathcal{H}_Q | \mathbf{x}_{k'} \rangle. \quad (8)$$

and assumed that the normalization $\langle \psi_\theta | \psi_\theta \rangle = 1$ is enforced by the ansatz, which is the case for the ARN we

implement. The energy (7) can be interpreted as the expectation $E = \mathbb{E}_{p(\mathbf{x}_k)} [E_{\text{loc}}(\mathbf{x}_k)]$ of the local energy over the wavefunction probability distribution, $p(\mathbf{x}_k) \equiv |\psi_\theta(\mathbf{x}_k)|^2$.

An unbiased estimate of this energy is given by the mean local energy across a batch of samples drawn from the underlying distribution defined by the wavefunction. Moreover, we can similarly use these samples to estimate the gradient of energy with respect to our variational parameters,

$$\nabla_\theta E = 2 \text{Re} (\mathbb{E}_p [E_{\text{loc}} \nabla_\theta \ln(\psi_\theta^*)]) \quad (9)$$

where, for brevity, we have dropped any explicit dependence on the state, \mathbf{x}_k . Therefore, to train the wavefunction, we can directly implement gradient descent towards the ground state using standard backpropagation techniques.

B. Autoregressive quantum states

Our choice of wavefunction ansatz is an autoregressive neural network — a class of generative models originally developed within the ML community as tractable, feed-forward alternatives to RBMs [27, 28] that have only very recently been demonstrated as viable NNQS in the context of condensed matter physics [15, 29]. The basic principle of an ARN is to decompose the joint probability distribution across multiple random variables z_i into a series of conditional distributions, e.g. $\text{pr}(z_1, \dots, z_n) = \prod_{i=1}^n \text{pr}(z_i | z_1, \dots, z_{i-1})$. That is to say, instead of trying to model the distribution over every possible configuration of these discrete variables simultaneously, one instead considers each variable sequentially, with each subsequent distribution being a function of the variables that have come before. Importantly, whilst an autoregressive model is still in principle universally expressive, it can, as we will see, permit highly efficient sampling.

In our case, the distribution we wish to model is a wavefunction over all N_O qubits with complex coefficients $\psi_k = e^{i\phi_k} |\psi_k\rangle$. As sampling a wavefunction only requires its absolute value we use an ARN only for $|\psi_k\rangle$. The overall phase, ϕ_k , is predicted separately by a standard feed-forward network that takes as input the entire configuration string.

The basis set of spin-orbitals used in our analysis consists of M spatial orbitals, each of which is doubly represented for the upward and downward projections of the spin, i.e. $N_O=2M$ and $|\mathbf{x}_k\rangle \equiv |x_k^{1\uparrow}, x_k^{1\downarrow}, \dots, x_k^{M\uparrow}, x_k^{M\downarrow}\rangle$. This leads to natural symmetries in the resulting wavefunction, as we discuss below, and so in constructing the network we choose to treat each of these spatial orbitals as a single unit, $v_k^i \equiv (x_k^{i\uparrow}, x_k^{i\downarrow})$, which can take on four possible configurations: $(0, 0)$, $(0, 1)$, $(1, 0)$, $(1, 1)$. Concretely, we consider wavefunction coefficients in the form

$$\ln \psi_k = \sum_{i=1}^M \ln |\psi_i(v_k^i | v_k^1 \dots v_k^{i-1})| + i\phi(v_k^1 \dots v_k^M). \quad (10)$$

So long as each conditional distribution is normalised such that $\sum_{v_k^i \in \{(0,0), (0,1), (1,0), (1,1)\}} |\psi_i(v_k^i | \dots)|^2 = 1$, the overall wavefunction is also normalised, $\sum_k |\psi_k|^2 = 1$.

C. Inference and efficient sampling

Our network architecture is shown in Fig. 1. The autoregressive property is realised by setting up M sub-networks, whose structure is shown in Fig. 2. The i -th sub-network takes the partial configuration string $(v_k^1 \dots v_k^{i-1})$ as input and outputs the log-amplitudes $\ln |\psi_i(v_k^i | v_k^1 \dots v_k^{i-1})|$ of the four possible configurations of v_k^i . The network can be used in two different modes which we refer to as ‘inference’ and ‘sampling’. Inference refers to the task of evaluating the log-amplitudes of a given configuration string, \mathbf{x}_k , and corresponds to a single forward pass of the network. In this setting, all sub-networks can run in parallel and their outputs are added according to Eq. (10).

The task of sampling is to generate configuration

Algorithm 1: Batched sampling procedure

```

input : batch size,  $N$ .
output: unique samples,  $X$ , their count,  $N_X$ , and their
         log-probability amplitudes,  $\ln \psi(\cdot)$ 
begin
  //  $X$  : partially sampled configurations
  //  $N_X$  : count of elements of  $X$ 
  //  $A$  : log prob. amp. for elements of  $X$ 
  initialise:  $X = [[]]$ ,  $N_X = [N]$ ,  $A = [0]$ 
  for each orbital  $i = 1, \dots, M$  do
    // Orbitals are processed sequentially.
    initialise:  $X^i = []$ ,  $N_X^i = []$ ,  $A^i = []$ 
    for  $k = 1, \dots, \text{len}(X)$  do
      // Samples are processed in parallel.
       $[v_k^1, \dots, v_k^{i-1}]$ ,  $n_k$ ,  $\ln \psi_k = X[k]$ ,  $N_X[k]$ ,  $A[k]$ 
      sub-network  $i$  forward pass:
       $\ln |\psi_i(\cdot | v_k^1 \dots v_k^{i-1})|$ 
      take  $n_k$  samples:  $v_k^i \sim |\psi_i(\cdot | v_k^1 \dots v_k^{i-1})|^2$ 
      for  $v_k^i$  sampled  $n_k^i$  times do
        if  $n_k^i > 0$  then
           $X^i.append([v_k^1, \dots, v_k^{i-1}, v_k^i])$ 
           $N_X^i.append(n_k^i)$ 
           $A^i.append(\ln |\psi_k| + \ln |\psi_i(v_k^i | v_k^1 \dots v_k^{i-1})|)$ 
        end
      end
    end
   $X \leftarrow X^i$ 
   $N_X \leftarrow N_X^i$ 
   $A \leftarrow A^i$ 
end
   $\ln \psi(X) = A + i\phi(X)$ 
  return  $X$ ,  $N_X$ ,  $\ln \psi(X)$ 
end

```

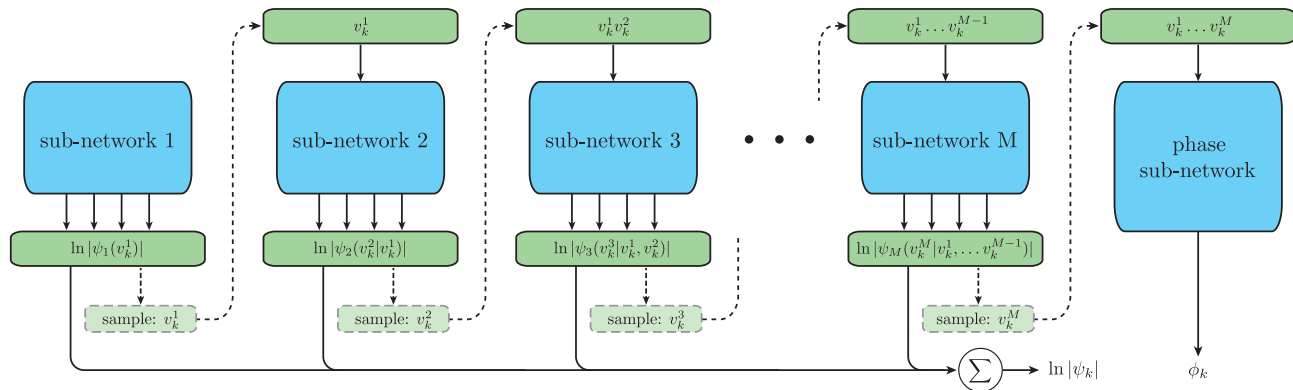


FIG. 1. The high level architecture of the ARN implementing our wavefunction ansatz. Solid lines indicate the operations used for the inference of the absolute value $|\psi_k|$ of the Slater determinant $|\mathbf{x}_k\rangle$. Blue blocks correspond to neural network operations, whose structure is further detailed in Fig. 2.

strings \mathbf{x}_k according to the underlying distribution $|\psi\rangle^2$. The procedure is detailed in Algorithm 1. The output of the i -th sub-network is used to sample a single pair of qubits v_k^i , which are then supplied, along with the previously acquired samples of v_k^1, \dots, v_k^{i-1} , to the next sub-network. When sampling multiple configurations, probability distribution over the next pair of qubits need only be evaluated once for every *unique* configuration of orbitals already sampled, which can be parallelised into a single batched forward-pass of the corresponding sub-network.

This sampling procedure has multiple highly desirable properties.

- (i) The computational cost of generating both a sample and its associated wavefunction coefficient is the same as a single forward pass of the full network during inference.
- (ii) A batch of exact and i.i.d. samples can be drawn from underlying distribution in parallel.
- (iii) The practical cost of generating a batch of samples scales with the number of unique configurations sampled, as opposed to the overall sample batch size.

Point (iii) is especially beneficial when sampling highly asymmetric systems — those where a single or few basis elements dominate the underlying distributions. This is exactly the case we find in quantum chemistry where the Hartree-Fock state typically dominates the low energy wavefunctions and will therefore be repeatedly sampled. As a result, obtaining meaningful statistics with which to optimise the wavefunction to below the Hartree-Fock energy requires massive numbers of samples where each batch will typically contain orders of magnitude fewer unique states.

Properties (i)-(iii) are a significant departure from the standard MCMC [30] algorithms commonly used to sample variationally optimised ansatz [14]. These approaches

rely on multiple sequential evaluations of proposed configurations, with the computational cost increasing with the required sample set quality and the total number of samples (rather than the number of unique samples). When applying RBMs to quantum chemistry using a Metropolis sampling scheme [31], Choo *et al.* [22] observed that performance depended strongly on the number of samples used, but were limited to maximum batch sizes of 10^6 . By contrast, our autoregressive ansatz readily generates batch sizes of up to 10^{12} . Indeed, even larger batch sizes could be used but we found that either this did not improve performance or, as we will discuss, calculating the local energies for the increasing number of unique states generated became too computationally expensive.

D. Encoding physical constraints

We treat the molecule as a system of N_O qubits, with the corresponding Hilbert space dimension being 2^{N_O} . A naive NNQS ansatz will predict nonzero probability for each of the 2^{N_O} basis configurations $(x_k^1, \dots, x_k^{N_O})$. However, only a small fraction of these configurations correspond to physically viable Slater determinants, particularly because the number of occupied spin-orbitals must equal the number N_e of electrons. Additional constraints arise from known physical symmetries and conservation laws.

Whilst the network could, in theory, learn over the course of training to excluding unphysical input vectors and output suitably symmetric distributions, it is desirable to have a network that incorporates these constraints in an *a priori* fashion. By keeping focused on a relatively small, physically meaningful subset of possible outputs, such a network helps streamline the training and reduce the computational costs.

Our autoregressive architecture satisfies this requirement, without sacrificing expressibility or sampling effi-

ciency, using the sub-network structure shown in Fig. 2. This structure combines computational processing by a trainable multi-level perceptron (MLP) with hard-coded pre-and post-processing that enforces the priors.

This capability is a further important advantage of ARNs with respect to other NNQS ansatz such as RBMs, which must instead rely on modified sampling methods to generate only physically viable states [22].

1. Conservation of electron number and multiplicity

The electron number and multiplicity of a molecule can be expressed as conserved quantities — N_e and $2S + 1$, respectively — both of which are known *a priori*. To utilize this information in our neural network, we first observe that we only need to consider determinants with the magnetic quantum number $|M_S| \leq S$. Moreover, due to the central symmetry of the problem, the energy of the molecule with a given total spin S does not depend on M_S , so it is sufficient to restrict ourselves to any single valid M_S [32]. In this work we choose $M_S=S$.

With this assumption, we can write for the total number of occupied spin-up, N_M^\uparrow , and spin-down, N_M^\downarrow , orbitals:

$$N_e = N_M^\uparrow + N_M^\downarrow, \quad S = M_S = (N_M^\uparrow - N_M^\downarrow)/2 \quad (11)$$

so $N_M^{\uparrow,\downarrow} = N_e/2 \pm S$. In order for a partial configuration string $(x_k^{1\uparrow}, x_k^{1\downarrow}, \dots, x_k^{i\uparrow}, x_k^{i\downarrow})$ processed by a i -th ARN subnetwork to be consistent with the conditions (11), it must satisfy the requirements

$$\begin{aligned} N_M^\uparrow - (M - i) &\leq N_i^{j\uparrow} \leq N_M^\uparrow, \\ N_M^\downarrow - (M - i) &\leq N_i^{j\downarrow} \leq N_M^\downarrow, \end{aligned} \quad (12)$$

where

$$N_i^\uparrow = \sum_{j=1}^i x_k^{j\uparrow}, \quad N_i^\downarrow = \sum_{j=1}^i x_k^{j\downarrow}. \quad (13)$$

We mask each ARN subnetwork's outputs to assign a zero probability (i.e. log-probability of negative infinity) to any partial configuration string that does not satisfy these conditions Eq. (12).

As a result of this simple modification, we achieve a remarkable reduction from the full 2^{N_O} possible qubit configurations to $\binom{M}{N_M^\uparrow} \binom{M}{N_M^\downarrow}$. We note that a similar technique was first used for NNQS by Allah *et al.* [16] but, to date, has only been used to enforce zero magnetisation in the context of CMP [16, 29].

2. Electron spin-flip symmetry

The electronic Hamiltonian (1) does not explicitly depend upon electron spin. Hence “flipping” every electron's spin should not change the absolute value of the

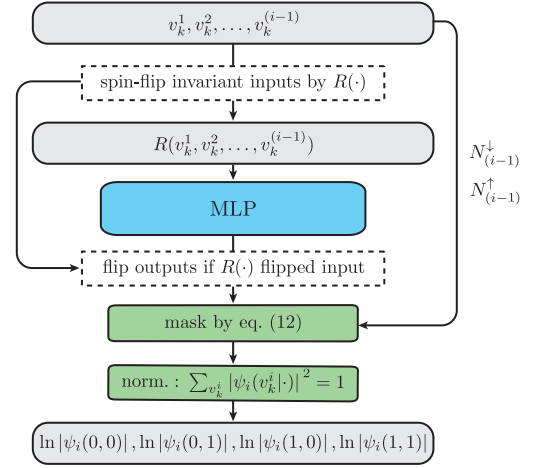


FIG. 2. The operation of a single conditional wavefunction sub-network. A multi-level perceptron (MLP) is the core of the sub-network, whose inputs and outputs are pre-and post-processes to enforce the physical prior: the conditional spin-flip $R(\cdot)$ ensures spin-flip symmetry as per Eq. (16), whilst the mask eliminates unphysical configurations that do not conserve the electron number and multiplicity.

amplitude associated with any specific Slater determinant. Concretely, defining this flipping operation as

$$F: |x_k^{1\uparrow}, x_k^{1\downarrow}, \dots, x_k^{M\uparrow}, x_k^{M\downarrow}\rangle \rightarrow |x_k^{1\downarrow}, x_k^{1\uparrow}, \dots, x_k^{M\downarrow}, x_k^{M\uparrow}\rangle, \quad (14)$$

we desire an ansatz such that $|\psi(\mathbf{x}_k)| = |\psi(F(\mathbf{x}_k))|$.

To achieve this, we enforce the equivalent symmetry onto *each* sub-network, such that each conditional wavefunction satisfies

$$|\psi_i(v_k^i | v_k^1 \dots v_k^{(i-1)})| = |\psi_i(F(v_k^i) | F(v_k^1 \dots v_k^{(i-1)}))|. \quad (15)$$

To that end, we pre-process the subnetwork input prior to entering it into the MLP, and post-process the MLP output as follows.

Recall that each sub-network has four outputs corresponding to the four possible configurations of $v_k^i \in \{(0,0), (0,1), (1,0), (1,1)\}$. Applying $F(\cdot)$ to the network output is then simply swapping the predictions for the pair of singly-occupied states. In the case that the input is spin-flip invariant ($F(v_k^1 \dots v_k^{i-1}) = v_k^1 \dots v_k^{i-1}$), Eq. (15) requires that log-amplitude of these singly-occupied states are equal. This requirement is satisfied by assigning these log-amplitudes the same value at the post-processing stage.

To enforce the condition (15) for non-spin-symmetric inputs, we apply the following transformation to the sub-network MLP input:

$$\begin{aligned} R(v_k^1 \dots v_k^{i-1}) & \\ &= \begin{cases} (v_k^1 \dots v_k^{i-1}) & \text{if } n(v_k^1 \dots v_k^{i-1}) < n(F(v_k^1 \dots v_k^{i-1})) \\ F(v_k^1 \dots v_k^{i-1}) & \text{if } n(v_k^1 \dots v_k^{i-1}) > n(F(v_k^1 \dots v_k^{i-1})), \end{cases} \end{aligned} \quad (16)$$

where $n(v_k^1 \dots v_k^{i-1})$ is the binary number corresponding to the sequence $x_k^{1\uparrow}, x_k^{1\downarrow}, \dots, x_k^{i-1\uparrow}, x_k^{i-1\downarrow}$. In other words,

$R(\cdot)$ maps a pair of spin-symmetric sub-network inputs to the same string, making the MLP output invariant to flipping the subnetwork input. If the input configuration is such that it had to be flipped, a corresponding flipping operation is applied to the MLP output. Full implementation details of the above procedures are provided in the Methods.

The spin-flip symmetry is only meaningful for the molecules being optimised with $M_S=0$, as this is required for both \mathbf{x}_k and $F(\mathbf{x}_k)$ to be physically valid configurations. With our choice of $M_S=S$, this constraint could only be applied to closed shell molecules with $S=0$. Additionally, we would not have been able to apply the spin-flip symmetry if our basis of spin-orbitals did not restrict their spatial component to be independent of the electron spin (as generated by so called unrestricted Hartree-Fock methods).

III. RESULTS

We now investigate both the performance of our network across a range of molecules and the importance of particular aspects of our architecture. To avoid “cherry-picking” and provide a fair assessment of the efficacy of our approach, all results presented in this work use a single set of network hyperparameters and identical training procedures. Further details on these points, along with the molecular geometries, baseline QC calculations and links to the source code and experimental scripts are provided in the Methods.

A. Obtained molecular ground states

The full experimental results obtained are presented in Table I from which we can see that our neural autoregressive quantum state (NAQS) exhibits consistently strong performance on all molecules considered. As baseline approximate QC methods, we consider the Hartree-Fock energy (HF), CI with single and double excitations (CISD), and CC with up to both double (CCSD) and perturbative triple excitations (CCSD(T)).

The obtained NAQS energies approach or match the ground-truth FCI result on all molecules with up to 20 electrons and 28 spin-orbitals, even when the most sophisticated baselines do not. Indeed, our NAQS still outperforms CCSD and CISD on Li_2O which has >40 M physically valid basis determinants under the Jordan-Wigner transformation. An apparent exception is a lower energy for Li_2O provided by CCSD(T); however, this result is also below the FCI limit (and is thus unphysical). In contrast, the ARN ansatz guarantees physical validity of its output states. This is further illustrated in Fig. 3 where FCI-like accuracy is obtained for the energy surface of N_2 , even in regimes where the CC baselines fail. Ultimately, this highlights the high degree of correlations and entanglement the NAQS is capable.pdf of learning.

It is illuminating to compare these results to the best (and, indeed, only) previous work applying neural network quantum states to quantum chemistry in the second quantisation – the RBM-based ansatz of Choo *et al.* [22]. The largest system on which it surpasses coupled-cluster methods is C_2 (44.1 k determinants), with the sampling-limited performance on larger molecules beating CISD on a system with ~ 1.6 M determinants. Our ansatz scales to systems multiple orders of magnitude larger without a loss of performance, and, moreover, beats that of Ref. [22] on every molecule larger than H_2 , which is trivially solved by most methods (direct numerical comparisons can be found in the Supplemental Data).

The impressive scaling of our system is heavily reliant on the sampling procedure outlined in section II C, which allows large batch sizes (and thus accurate gradient estimates) without excessive computational overhead. The efficient optimisation this allows is evidenced by our “under-sampling” of the optimisation space for large molecules. Specifically, with (without) masking unphysical determinants, for LiCl and Li_2O we typically only sampled $\sim 28\%$ (20%) and $\sim 5\%$ (1%) of the physically viable determinants at least once during training, respectively, and still learnt the important configurations required for accurate wavefunctions. This suggests that the neural network is able to generalise to unseen configurations, and therefore offers a promising approach to efficiently exploring and isolating the important components of the entire optimisation space.

Moreover, we found that typically, after an initial pe-

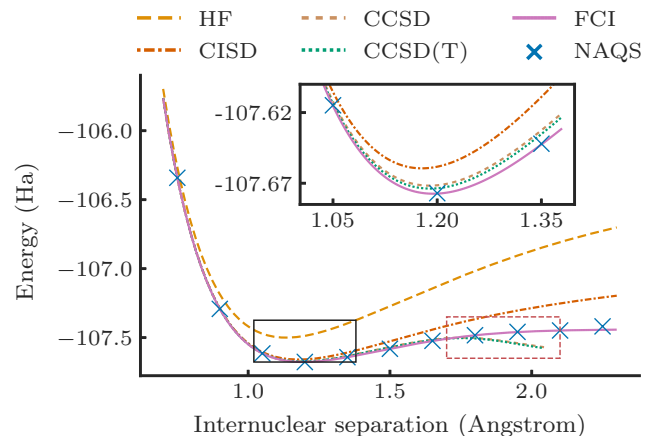


FIG. 3. Comparison of the energy obtained using a neural autoregressive quantum state (NAQS) to traditional QC approaches for the diatomic nitrogen molecule, as a function of the nuclear separation. The NAQS outperforms all other approximation techniques, almost exactly matching the ground-truth FCI solution in all cases, including near equilibrium (inset and solid black box) and even away from the equilibrium geometry where other methods — including the otherwise most accurate coupled-cluster approach — fail due to the presence of strong quantum correlations (highlighted with dashed-red box).

Molecular information					Method comparison						NAQS variants		
Molecule	N_O	N_e	S	Valid \mathbf{x}_k	HF	CISD	CCSD	CCSD(T)	NAQS	FCI	Standard	No mask	No spin sym.
H ₂	4	2	0	4	-0.9109	-0.9981	-0.9981	-0.9981	-0.9981	-0.9981	-0.9981	-0.9981	-0.9981
F ₂	20	18	0	100	-195.6380	-195.6611	-195.6611	-195.6611	-195.6611	-195.6611	-195.6611	-195.6611	-195.6611
HCl	20	18	0	100	-455.1360	-455.1562	-455.1562	-455.1562	-455.1562	-455.1562	-455.1562	-455.1562	-455.1562
LiH	12	4	0	225	-7.7674	-7.7845	-7.7845	-7.7845	-7.7845	-7.7845	-7.7845	-7.7845	-7.7845
H ₂ O	14	10	0	441	-74.964	-75.0148	-75.0151	-75.0155	-75.0155	-75.0155	-75.0155	-75.0155	-75.0155
CH ₂	14	8	1	735	-37.4846	-37.5044	-37.5044	-37.5044	-37.5044	-37.5044	-37.5044	-37.5044	-37.5044
O ₂	20	16	1	1200	-147.6319	-147.7502	-147.7477	-147.7485	-147.7500	-147.7502	-147.7500	-147.7496	-147.7500
BeH ₂	14	6	0	1225	-14.4432	-14.4725	-14.4727	-14.4729	-14.4729	-14.4729	-14.4729	-14.4729	-14.4729
H ₂ S	22	18	0	3025	-394.3114	-394.3539	-394.3546	-394.3546	-394.3546	-394.3546	-394.3546	-394.3546	-394.3546
NH ₃	16	10	0	3136	-55.4548	-55.5195	-55.5209	-55.5210	-55.5211	-55.5211	-55.5211	-55.5211	-55.5211
N ₂	20	14	0	14 400	-107.4990	-107.6471	-107.6561	-107.6579	-107.6595	-107.6602	-107.6595	-107.6588	-107.6511
CH ₄	20	10	0	15 876	-39.7266	-39.8035	-39.8060	-39.8062	-39.8062	-39.8063	-39.8062	-39.8061	-39.8061
C ₂	20	12	0	44 100	-74.4209	-74.6371	-74.6745	-74.6876	-74.6899	-74.6908	-74.6899	-74.6562	-74.6898
LiF	20	12	0	44 100	-105.1137	-105.1607	-105.1592	<i>-105.1663</i>	-105.1662	-105.1662	-105.1660	-105.1662	-105.1660
PH ₃	24	18	0	48 400	-338.6341	-338.6963	-338.6982	-338.6984	-338.6984	-338.6984	-338.6984	-338.6984	-338.6984
LiCl	28	20	0	1 002 001	-460.8273	-460.8482	-460.8476	<i>-460.8500</i>	-460.8496	-460.8496	-460.8496	-460.8496	-460.8496
Li ₂ O	30	14	0	41 409 225	-87.7956	-87.8837	-87.8855	<i>-87.8931</i>	-87.8909	-87.8927	-87.8878	-87.8909	-87.8867

TABLE I. Obtained molecular ground-state energies (in Ha) using various canonical methods and a variationally optimised NAQS (“Standard” following the procedure from the main text, along with associated ablations). Also provided is information for each molecule, including the number of physically valid determinants (Valid \mathbf{x}_k) remaining after reducing the optimisation space obtained using the Jordan-Wigner transform to conserve electron number, N_e , and total spin, S . All stochastic methods (NAQS and associated ablations) report the best result obtained across five optimisation attempts, with the exception of Li₂O for which only a single attempt was used due to the increased computational cost. The best non-FCI results are displayed in bold (with those matching FCI additionally underlined), excluding methods that produce unphysical energies below the FCI limit, which are displayed in italic.

riod of exploration, the ARN isolates a relatively small number of determinants that dominate the NAQS. The remainder of the optimization run is spent fine-tuning the amplitudes of these determinants. For example, even without apply a masking to restrict the ARN to only physically viable determinants, the final epoch of Li₂O generated 10^{12} samples distributed across only 13 761 unique determinants. If we take the subspace spanned by these determinants and simply diagonalise the Hamiltonian, we obtain an energy of -87.8911 Ha, which is even lower than that found by the ARN (-87.8909 Ha). This suggests a hybrid approach, where canonical numerical methods are applied to the subspace of configurations found by the network to achieve even lower energies. Further exploration of these ideas is left for future work.

B. Ablation studies

To examine the impact of encoding physical priors into the NAQS, Table I additionally includes results for two ablations. A NAQS with “No mask” can assign non-zero probability to, and thus sample, any of the 2^{N_O} possible configurations regardless of whether they are physically viable. “No spin sym.” indicates that the spin-flip invariance (15) is removed from the wavefunction. An exception is open-shell molecules (CH₂ and O₂), to which spin-flip invariance could not be applied; however, these molecules showed FCI-level performance even without this constraint.

Whilst we see that removing either of these physical

priors can result in a slight drop in performance, the effect appears subtle. However, when we consider the performance across multiple initialisations a clearer distinction is evident. Fig. 4 shows the energies obtained for every individual run, and the corresponding overall average performance, on the six largest molecules for which we performed multiple optimisations. We can see that the average performance of a NAQS is significantly improved when our physical knowledge is encoded into the system. Moreover, in the few cases that the best result is obtained by an ablation (for example, “No mask” on LiF) it is clear that this is the result of one fortuitous seed, rather than a systematic effect. Further numerical results on the average performance across multiple seeds are provided in the supplemental data.

In general, the effect of these ablations only becomes visible on larger systems, such as those shown in Fig. 4. This seems reasonable, as with the larger dimension of the Hilbert space the set of possible configuration strings grows exponentially, hence it becomes more critical to reduce its size with the known *a priori* constraints.

IV. DISCUSSION

In this work we have presented an ARN ansatz for *ab initio* QC that approaches FCI-quality solutions on systems with up to 30 spin orbitals, even in situations where canonical approximation methods fail. This success is attributable to both the ability to embed physical priors into the network — specifically, spin-flip invariance, and

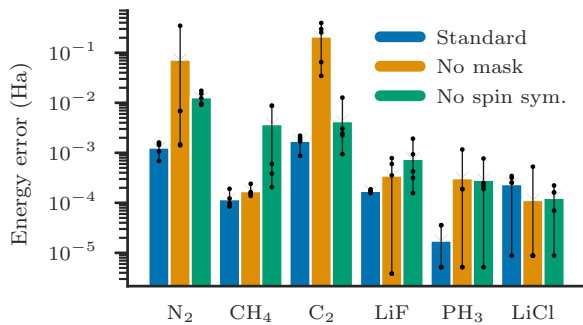


FIG. 4. The variational energies obtained over the course of optimisation for the NAQS model described in the text (“Standard”) and the associated ablations of both restricting the optimisation space to physically viable determinants (“No mask”) and the spin-flip symmetries of the final wavefunction (“No spin sym.”). Each bar denotes the average performance across the 5 training seeds, with the dots denoting the energies obtained by individual runs and the vertical black line indicating the span from the best to worst of these. Where fewer than 5 dots are visible, this is due the same energy being found multiple times. Energies are plotted in terms of their “error”, the distance from the ground-truth FCI energy, on a logarithmic scale.

conservation of electron number and total spin — and an efficient sampling procedure that scales with the number of unique configurations sampled, rather than the total batch size. These advances ultimately allow our approach to scale to systems multiple orders of magnitude larger than was previously possible in ML-based approaches to second quantised QC [22].

This work addresses the requirement for an efficient and expressive ansatz, with the remaining barrier to even larger molecules being the computational cost of VMC calculations separate from neural network itself. Given a batch of N_{unq} unique samples, calculating the associated local energies as per Eq. (8) scales as $\mathcal{O}(N_{\text{O}}^4 \times N_{\text{unq}})$ for second-quantised QC Hamiltonians [5], \mathcal{H}_{Q} . Although the $\mathcal{O}(N_{\text{O}}^4)$ matrix elements in that Hamiltonian can in principle be calculated on-demand, and then cached, using the efficient algorithm described in Ref. [22], this calculation remains a significant computational expense for large molecules. Whilst increasingly optimised implementations run with more compute would allow our approach to be pushed further, an interesting alternative would be to search for efficient methodologies for calculating expectation values directly from the NNQS parameters, which would help address the computational challenges both in QC and beyond.

It is also important to note that the fundamental accuracy of a second-quantised approach is limited by the choice of basis set, with the challenges associated with scaling to larger basis sets equivalent to those of scaling to larger molecules discussed above. However, very recent work has shown that neural networks can also be used to express the ground state wavefunctions in considerably

fewer determinants [33, 34]. Thus even higher accuracies can be obtained by optimising the basis set, albeit at the expense of increased computational complexity. Whilst these approaches both use MCMC sampling, their compatibility with our second-quantized picture is not clear, however this comparison remains an interesting prospect for future research.

Ab initio QC, with its long range interactions, bespoke physical symmetries and conservation laws, represents a significant new challenge for NNQS as compared to e.g., CMP, in which problems are often characterised by periodic structure and local interactions [14–16]. Our work further demonstrates that techniques developed within CMP and ML can be applied to more challenging systems and offer viable alternatives to traditional methods. It represents one of the most ambitious applications of NNQS to date.

ACKNOWLEDGEMENTS

The authors are grateful to G. Carleo for his insights regarding RBMs, and to M. Sapova for her assistance with quantum chemical calculations. A.L.’s research is partially supported by Russian Science Foundation (19-71-10092).

CODE AVAILABILITY

Source code for this work, including experimental scripts and molecular data required to reproduce the reported results, can be found at <https://github.com/tomdbar/naqs-for-quantum-chemistry>.

METHODS

Mapping fermionic Hamiltonians to the qubits

We consider the second quantised form of the molecular electronic Hamiltonian [5],

$$\mathcal{H} = \sum_{p,q} h_{pq} \hat{a}_p^\dagger \hat{a}_q + \frac{1}{2} \sum_{p,q,r,s} h_{pqrs} \hat{a}_p^\dagger \hat{a}_q^\dagger \hat{a}_r \hat{a}_s, \quad (17)$$

where \hat{a}_i^\dagger (\hat{a}_i) is fermionic electron creation (annihilation) operator for the i -th single-electron orbital and h_{pq} , h_{pqrs} are the one- and two-body integrals, respectively. We use the Jordan-Wigner encoding [26] to map from operators acting on indistinguishable fermions to operators acting on distinguishable qubits. This is given by

$$\hat{a}_j^\dagger \rightarrow \left(\prod_{i=0}^{j-1} \sigma_i^z \right) \sigma_j^+, \quad \hat{a}_j \rightarrow \left(\prod_{i=0}^{j-1} \sigma_i^z \right) \sigma_j^-, \quad (18)$$

which stores the occupation state of the j -th fermionic mode locally in the j -th qubit — using the raising/lowering operator $\sigma_j^\pm = \sigma_j^x \pm i\sigma_j^y$ — whilst the parity is stored non-locally. Whilst other mappings that differently store the occupation and parity of fermionic modes could be used — such as the

parity [35] or Bravyi-Kitaev [36] encodings — these would each require bespoke consideration of how to encode physical priors into our system. Regardless of the choice of encoding, the qubit Hamiltonian still takes the form of Eq. (5) from the main text.

Network architecture

All results presented in this work use a single set of network hyperparameters. Each subnetwork, $\ln |\psi_i(v_k^i | v_k^1, \dots, v_k^{i-1})|$, uses an MLP with a single hidden layer of 64 neurons with the single phase network, $\phi(\cdot)$, using two hidden layers of 512 neurons. Both networks use ReLU activations [37] on all hidden layers, with no activation on the input or output layers. We emphasise that this architecture is massively overparameterised for most, if not all, of the molecules we consider. However, the forward and backward pass of the network are not our computational bottleneck (as discussed, it was the calculation of matrix-elements of the Hamiltonian) and therefore optimising the network size was not considered.

The autoregressive wavefunction decomposition defined in Eq. (10) does leave a degree of freedom in the form of the order of our conditional wavefunctions. In this work, we consider orbitals in order of decreasing energy, i.e. $\ln \psi_1(\cdot)$ and $\ln \psi_M(\cdot)$ correspond to the highest and lowest energy orbitals, respectively. Optimal ordering of the spin-orbitals in a NAQS can be an interesting subject for future research.

To ensure the conditional wavefunction have spin-flip symmetry as defined in Eq. (15) of the main text, we first split the input to the i -th subnetwork into its spin-up and spin-down orbitals: $(x_k^{1\uparrow}, \dots, x_k^{(i-1)\uparrow})$ and $(x_k^{1\downarrow}, \dots, x_k^{(i-1)\downarrow})$. Recalling that $x_k \in \{0, 1\}$, we can consider each of these partially sampled configurations as a binary-encoded integer.

The input to each sub-network is therefore invariant to global spin flips, so we next have to reconstruct the desired symmetries at the output. Concretely, the MLP outputs 5 values

$$\text{MLP}_i(R(v_k^1 \dots v_{i-1}^k)) = [z_1, z_2, z_3, z_4, z_5], \quad z_j \in \mathbb{R}, \quad (19)$$

which we convert to four unnormalised log-probability amplitudes for the value of the next pair of qubits. If we have a spin-symmetric input ($F(v_k^1 \dots v_{i-1}^k) = (v_k^1 \dots v_{i-1}^k)$), then the outputs are simply

$$\begin{aligned} \ln |\tilde{\psi}_i(0, 0)| &= z_1 \\ \ln |\tilde{\psi}_i(0, 1)| &= z_2 \\ \ln |\tilde{\psi}_i(1, 0)| &= z_2 \\ \ln |\tilde{\psi}_i(1, 1)| &= z_3 \end{aligned}$$

(where the tilde indicates that the amplitudes are not normalized). However, if the input is not spin-symmetric ($F(v_k^1 \dots v_{i-1}^k) \neq (v_k^1 \dots v_{i-1}^k)$), then the outputs are

$$\begin{aligned} \ln |\tilde{\psi}_i(0, 0)| &= z_1 \\ \ln |\tilde{\psi}_i(0, 1)| &= \begin{cases} (z_2+z_4)/2 & \text{if } n(v_k^1 \dots v_k^{i-1}) < n(F(v_k^1 \dots v_k^{i-1})) \\ (z_2+z_5)/2 & \text{if } n(v_k^1 \dots v_k^{i-1}) > n(F(v_k^1 \dots v_k^{i-1})) \end{cases} \\ \ln |\tilde{\psi}_i(1, 0)| &= \begin{cases} (z_2+z_5)/2 & \text{if } n(v_k^1 \dots v_k^{i-1}) < n(F(v_k^1 \dots v_k^{i-1})) \\ (z_2+z_4)/2 & \text{if } n(v_k^1 \dots v_k^{i-1}) > n(F(v_k^1 \dots v_k^{i-1})) \end{cases} \\ \ln |\tilde{\psi}_i(1, 1)| &= z_3. \end{aligned}$$

These definitions satisfy the symmetries discussed in the main text. Namely, a spin-symmetric input ($F(v_k^1 \dots v_{i-1}^k) = (v_k^1 \dots v_{i-1}^k)$) should have spin-symmetric outputs, and that a pair of spin-symmetric inputs should have correspondingly symmetric outputs. Of course, there are many choices for how to combine or permute outputs of an MLP to achieve these effects, with the above being what we found to work best in practice.

Training details

The network can be trained by following the gradients defined in Eq. (9). However, the variance of the gradients can be reduced, without introducing any bias into the sample approximation, by subtracting a baseline [16],

$$\nabla_{\theta} E = 2 \text{Re} \left(\mathbb{E}_p \left[(E_{\text{loc}} - \mathbb{E}_p[E_{\text{loc}}]) \nabla_{\theta} \ln(\psi^*) \right] \right). \quad (20)$$

This improves training stability and is a standard technique deployed in machine learning to improve gradient estimation [38, 39].

Training follows the standard VMC approach described in the main text, with all parameters simultaneously optimised using the Adam algorithm [40] with an initial learning rate of 5×10^{-3} , dropped to 5×10^{-4} halfway through training, and decay rates for the first- and second-moment estimates of $\beta_1 = 0.9$ and $\beta_2 = 0.99$, respectively. The number of samples (N in algorithm 1) used to estimate the stochastic gradient steps, Eq. (20), was automatically adjusted to ensure the number of unique physically valid samples remained between 10 k and 100 k for as long as possible. Specifically, the initial batch size of 10^6 was increased/decreased by an order of magnitude whenever the additional/fewer unique samples were required, with an upper batch size limit of 10^{12} .

The random initialisation of the network parameters (which was not modified from the default behaviour of PyTorch and can be found in the supporting code) does impact final performance, therefore to avoid ‘‘cherry-picking’’, all reported results are the best energy obtained across exactly 5 seeds, each trained for 10k steps, with the exception of Li_2O which uses only a single seed due to the increased computational cost.

Molecular geometries and calculations

The molecular geometries used are the geometries in the STO-3G basis returned from the PubChem [41] database by OpenFermion [42]. OpenFermion was also used to generate qubit Hamiltonians of the form of Eq. (5), with the back-end calculations and baseline QC methods – HF, CI, CCSD, CCSD(T) — implemented using Psi4 [43]. Exact geometries and scripts to reproduce all of these steps can be found in supporting code.

-
- [1] M. Troyer and U.-J. Wiese, Phys. Rev. Lett. **94**, 170201 (2005).
- [2] B. L. Hammond, W. A. Lester, and P. J. Reynolds, *Monte Carlo methods in ab initio quantum chemistry*, Vol. 1 (World Scientific, 1994).
- [3] S. Langhoff, *Quantum mechanical electronic structure calculations with chemical accuracy*, Vol. 13 (Springer Science & Business Media, 2012).
- [4] L. Piela, *Ideas of quantum chemistry* (Elsevier, 2013).
- [5] S. McArdle, S. Endo, A. Aspuru-Guzik, S. C. Benjamin, and X. Yuan, Rev. Mod. Phys. **92**, 015003 (2020).
- [6] C. D. Sherrill and H. F. Schaefer III, in *Advances in quantum chemistry*, Vol. 34 (Elsevier, 1999) pp. 143–269.
- [7] F. Coester and H. Kümmel, Nucl. Phys. **17**, 477 (1960).
- [8] R. J. Bartlett and M. Musiał, Rev. Mod. Phys. **79**, 291 (2007).
- [9] W. Foulkes, L. Mitas, R. Needs, and G. Rajagopal, Rev. Mod. Phys. **73**, 33 (2001).
- [10] S. R. White, Phys. Rev. Lett. **69**, 2863 (1992).
- [11] S. R. White and R. L. Martin, J. Chem. Phys. **110**, 4127 (1999).
- [12] M. P. Nightingale and C. J. Umrigar, *Quantum Monte Carlo methods in physics and chemistry*, 525 (Springer Science & Business Media, 1998).
- [13] E. Neuscamman, H. Changlani, J. Kinder, and G. K.-L. Chan, Phys. Rev. B **84**, 205132 (2011).
- [14] G. Carleo and M. Troyer, Science **355**, 602 (2017).
- [15] O. Sharif, Y. Levine, N. Wies, G. Carleo, and A. Shashua, Phys. Rev. Lett. **124**, 020503 (2020).
- [16] M. Hibat-Allah, M. Ganahl, L. E. Hayward, R. G. Melko, and J. Carrasquilla, Phys. Rev. Research **2**, 023358 (2020).
- [17] G. Torlai, G. Mazzola, J. Carrasquilla, M. Troyer, R. Melko, and G. Carleo, Nature Phys. **14**, 447 (2018).
- [18] J. Carrasquilla, G. Torlai, R. G. Melko, and L. Aolita, Nat. Mach. Intell. **1**, 155 (2019).
- [19] M. Neugebauer, L. Fischer, A. Jäger, S. Czischek, S. Jochim, M. Weidemüller, and M. Gärtner, Phys. Rev. A **102**, 042604 (2020).
- [20] S. Ahmed, C. S. Muñoz, F. Nori, and A. F. Kockum, arXiv:2008.03240 (2020).
- [21] B. Jónsson, B. Bauer, and G. Carleo, arXiv:1808.05232 (2018).
- [22] K. Choo, A. Mezzacapo, and G. Carleo, Nature Commun. **11**, 1 (2020).
- [23] Y. LeCun, D. Touresky, G. Hinton, and T. Sejnowski, in *Proceedings of the 1988 connectionist models summer school*, Vol. 1 (1988) pp. 21–28.
- [24] X. Gao and L.-M. Duan, Nature Commun. **8**, 1 (2017).
- [25] K. Choo, T. Neupert, and G. Carleo, Phys. Rev. B **100**, 125124 (2019).
- [26] E. Wigner and P. Jordan, Z. Phys **47**, 631 (1928).
- [27] H. Larochelle and I. Murray, in *Proceedings of the Fourteenth International Conference on Artificial Intelligence and Statistics* (2011) pp. 29–37.
- [28] B. Uria, M.-A. Côté, K. Gregor, I. Murray, and H. Larochelle, J. Mach. Learn. Res. **17**, 7184 (2016).
- [29] S. Morawetz, I. J. De Vlucht, J. Carrasquilla, and R. G. Melko, arXiv:2010.14514 (2020).
- [30] S. Brooks, A. Gelman, G. Jones, and X.-L. Meng, *Handbook of markov chain monte carlo* (CRC press, 2011).
- [31] W. K. Hastings, *Monte Carlo sampling methods using Markov chains and their applications* (Oxford University Press, 1970).
- [32] C. D. Sherrill, <http://vergil.chemistry.gatech.edu/notes/ci.pdf> (1995).
- [33] D. Pfau, J. S. Spencer, A. G. d. G. Matthews, and W. M. C. Foulkes, arXiv:1909.02487 (2019).
- [34] J. Hermann, Z. Schätzle, and F. Noé, arXiv:1909.08423 (2019).
- [35] J. T. Seeley, M. J. Richard, and P. J. Love, J. Chem. Phys. **137**, 224109 (2012).
- [36] S. B. Bravyi and A. Y. Kitaev, Ann. Phys. (N. Y.) **298**, 210 (2002).
- [37] X. Glorot, A. Bordes, and Y. Bengio, in *Proceedings of the fourteenth international conference on artificial intelligence and statistics* (2011) pp. 315–323.
- [38] R. S. Sutton and A. G. Barto, *Reinforcement learning: An introduction* (MIT press, 2018).
- [39] S. Mohamed, M. Rosca, M. Figurnov, and A. Mnih, arXiv:1906.10652 (2019).
- [40] D. P. Kingma and J. Ba, arXiv:1412.6980 (2014).
- [41] S. Kim, P. A. Thiessen, E. E. Bolton, J. Chen, G. Fu, A. Gindulyte, L. Han, J. He, S. He, B. A. Shoemaker, et al., Nucleic Acids Res. **44**, D1202 (2016).
- [42] J. McClean, N. Rubin, K. Sung, I. D. Kivlichan, X. Bonet-Monroig, Y. Cao, C. Dai, E. S. Fried, C. Gidney, B. Gimby, et al., Quantum Sci. Technol. (2020).
- [43] D. G. Smith, L. A. Burns, A. C. Simmonett, R. M. Parrish, M. C. Schieber, R. Galvelis, P. Kraus, H. Kruse, R. Di Remigio, A. Alenaizan, et al., J. Chem. Phys. **152**, 184108 (2020).

SUPPLEMENTAL DATA

Molecular information						NAQS ablations		
Molecule	N_O	N_e	S	Valid \mathbf{x}_k	FCI	Full mask	No mask	No spin sym.
H ₂	4	2	0	4	-0.9981	-0.9981	-0.9981	-0.9981
F ₂	20	18	0	100	-195.6611	-195.6605(12)	-195.6579(48)	-195.660(1)
HCl	20	18	0	100	-455.1562	-455.1562	-455.1561(1)	-455.1562
LiH	12	4	0	225	-7.7845	-7.7845	-7.7845	-7.7845(7)
H ₂ O	14	10	0	441	-75.0155	-75.0155	-75.0155	-75.0155
CH ₂	14	8	1	735	-37.5044	—	-37.33(23)	-37.5041(4)
O ₂	20	16	1	1200	-147.7502	—	-147.70(92)	-147.747(3)
BeH ₂	14	6	0	1225	-14.4729	-14.4729	-14.4729	-14.471(3)
H ₂ S	22	18	0	3025	-394.3546	-394.3546	-394.35(13)	-394.3546
NH ₃	16	10	0	3136	-55.5211	-55.5211	-55.5211	-55.5211(1)
N ₂	20	14	0	14 400	-107.6602	-107.6589(4)	-107.65(15)	-107.647(4)
CH ₄	20	10	0	15 876	-39.8063	-39.8061	-39.8061	-39.803(5)
C ₂	20	12	0	44 100	-74.6908	-74.6891(5)	-74.48(15)	-74.687(5)
LiF	20	12	0	44 100	-105.1662	-105.1660	-105.1658(3)	-105.1654(7)
PH ₃	24	18	0	48 400	-338.6984	-338.6984	-338.6981(5)	-338.6981(3)
LiCl	28	20	0	1 002 001	-460.8496	-460.8494(1)	-460.8495(2)	-460.8495(1)

TABLE I. Average molecular ground-state energies (in Ha) of different NAQS configurations as described in the main text. Averages are across 5 seeds with brackets denoting the standard deviation across all seeds on the final digits. Where no uncertainty is denoted, the variation is below the level of precision reported in the table. Notably large uncertainties, such as ‘No mask’ for CH₂ and ‘Partial mask’ for C₂ are the result of rare failure seeds, where a single run of NAQS fails to converge to a meaningful energy. The ‘missing’ entries for CH₂ and O₂ indicate that we do not enforce spin-symmetry to these systems as discussed in the main text. Also provided is information for each molecule, including the number of physically valid determinants (Valid \mathbf{x}_k) remaining after reducing the optimisation space obtained using the Jordan-Wigner transform to conserve electron number, N_e , and total spin, S . The best results are displayed in bold (with those matching FCI additionally underlined).

Molecule	Classical methods				NNQS		FCI
	HF	CISD	CCSD	CCSD(T)	RBM	NAQS	
H ₂	-1.1170	-1.1373	-1.1373	-1.1373	-1.1373	-1.1373	-1.1373
LiH	-7.8631	-7.8827	-7.8828	-7.8828	-7.8826	-7.8828	-7.8828
H ₂ O	-74.9625	-75.0221	-75.0231	-75.0232	-75.0232	-75.0233	-75.0233
NH ₃	-55.4513	-55.5258	-55.5280	-55.5281	-55.5277	-55.5282	-55.5282
N ₂	-107.4912	-107.6591	-107.6717	-107.6738	-107.6767	-107.6774	-107.6774
C ₂	-74.4209	-74.6371	-74.6745	-74.6876	-74.6892	-74.6895	-74.6908

TABLE II. Comparison of the performance a NAQS and an RBM. NAQS results were obtained by following the exact same procedure as described for the results in the main text. RBM results are as reported by Choo *et al.* in reference [22] of the main text. The best results are displayed in bold (with those matching FCI additionally underlined). Note that the molecular geometries match those from [22], which differ from those presented in Table 1 of the main text, hence the different FCI energies for the same species of molecule.

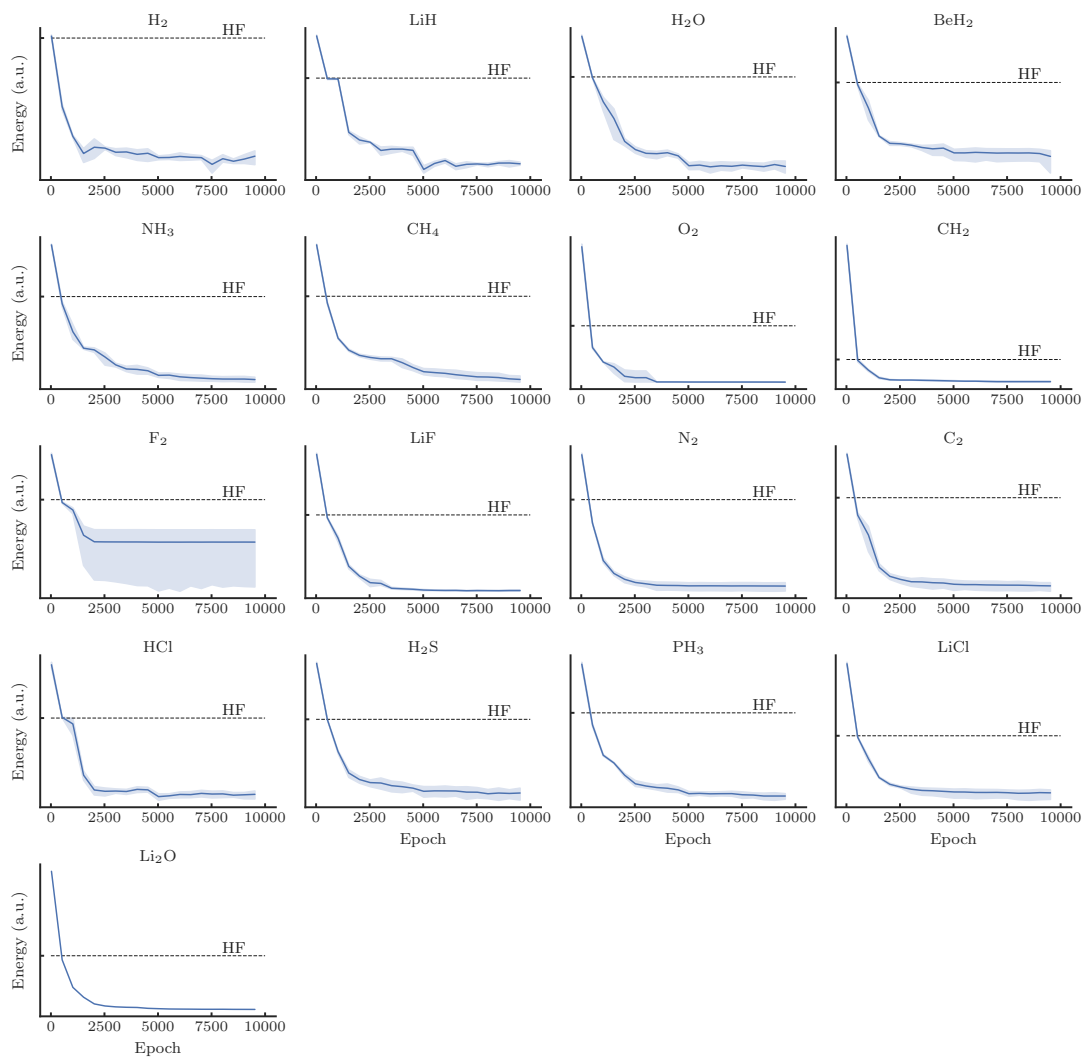


FIG. 1. The variation energies obtained over the course of optimisation using the standard network architecture presented in the main text. Where possible, the results are averaged across all five training seeds, with the shaded regions denoting the 95% confidence interval. For Li_2O , the single optimisation attempt for each network configuration is displayed. All plots use logarithmic scaling on the energy axis, with a dashed horizontal line denoting the Hartree-Fock (HF) energy.